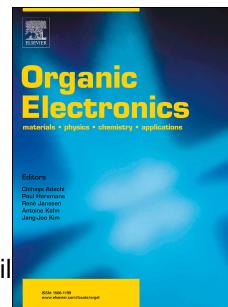# Accepted Manuscript

Local anodic oxidation lithography on organic semiconductor crystals: Oxide depth revealed by conductance tomography

Muhammad S. Kamaludin, Robert J. Thompson, Steve Hudziak, Oleg Mitrofanov, Neil J. Curson

Please cite this article as: M.S. Kamaludin, R.J. Thompson, S. Hudziak, O. Mitrofanov, N.J. Curson, Local anodic oxidation lithography on organic semiconductor crystals: Oxide depth revealed by conductance tomography, *Organic Electronics* (2018), doi: https://doi.org/10.1016/j.orgel.2018.09.041.

Insulating oxide line drawn using AFM-based anodic oxidation

Conductive AFM tip ploughs into substrate while imaging, producing a crater that reveals oxide line depth

36 pA

20

−2

500 nm

Scan no. 1
2.3 min

20
45 min

41
92 min

47
107 min

48
109 min

50
112 min

53
118 min

Local anodic oxidation lithography on organic semiconductor crystals: oxide depth revealed by conductance tomography

Muhammad S. Kamaludin [a,b,*], **Robert J. Thompson** [c], **Steve Hudziak** [c], **Oleg Mitrofanov** [c], **and Neil J. Curson** [a,c]

[a] London Centre for Nanotechnology, 17-19 Gordon Street, London WC1H 0AH, United Kingdom
[b] Department of Physics and Astronomy, University College London, Gower Street, London WC1E 6BT, United Kingdom
[c] Department of Electronic & Electrical Engineering, Roberts Building, University College London, Torrington Place, London WC1E 7JE, United Kingdom
[*] Corresponding author: muhammad.kamaludin.10@ucl.ac.uk

ABSTRACT

Nanopatterning electrically insulating oxide lines on organic electronic surfaces can play a role in fabricating future nanoscale devices. Here we write oxide features on rubrene single crystal surfaces by performing local anodic oxidation using the tip of an atomic force microscope. Oxide feature height increases with voltage bias and decreases with tip writing speed, and gaps as small as 22 nm at the surface between two parallel oxide lines were realised. Conductance tomography is employed in a unique way to determine the depths of oxide features, by exposing subsurface layers of the patterned material without using chemical etching while simultaneously mapping material conductance. The oxide line depth exceeds its height, with the depth-to-height ratio frequently being more than 1.6. A critical electric field of ~3×10^6 V/cm is identified, below which the oxide growth ceases, resulting in a maximum oxide vertical extent of about ~60 nm at a voltage bias of ~20 V.

1. Introduction

Organic electronic materials have a number of unique properties, enabling the formation of flexible electronics [1], chemical tuning to produce desired device properties [2], and the potential for cost-effective device mass production [3]. Developing capabilities to pattern and modify the surface of these materials to improve device architectures and make future devices is an important technological requirement [4]. Local anodic oxidation (LAO) lithography [5] is a possible route for organic nanoscale (e.g. one-dimensional) device fabrication, as this direct-write and resistless technique can be used to draw narrow insulating oxide lines on surfaces to precisely define shapes and dimensions. Upscaling for large-scale/mass fabrication is possible, as demonstrated on silicon using template stamps [6], and a potential application is in increasing organic electronic device density on a shared active material by patterning electrically insulating barriers to prevent cross-talk between adjacent devices. However, little is reported about locally oxidising crystalline organic semiconductor substrates, though related works are noted, such as on-demand patterning of polycrystalline pentacene field-effect transistors by thermal scanning lithography [7], nano-scratching of PEDOT:PSS electrodes [8] and LAO patterning on pentacene thin films to direct antibody deposition [9]. Thus, motivated by the promising potential for future organic electronic device fabrication, LAO using atomic force microscopy (AFM) is investigated on ultrapure rubrene single crystals for the first time.

Rubrene is considered the prototype single crystal organic semiconductor because of its relatively large charge carrier mobility (10-40 cm^2/(V·s)) [10–12] and long exciton diffusion lengths (~4 microns) [13,14]. Oxidation properties of the single crystal have been studied in detail; in addition to evidence of an epitaxial native oxide layer [15], oxygen-related species have been observed uniformly on the surface and preferentially at structural defects [16], as well as under the surface [17], having accessed preferential channels into the bulk before spreading laterally [18]. Meanwhile, multiple oxygen incorporation mechanisms have been proposed, each with unique oxygen exposure methods, suggesting varying effects on rubrene device performance. Some hold the opinion that (photo)conductivity and field-effect mobility of rubrene devices are increased [19–21] while others have the opposite opinion [22,23].
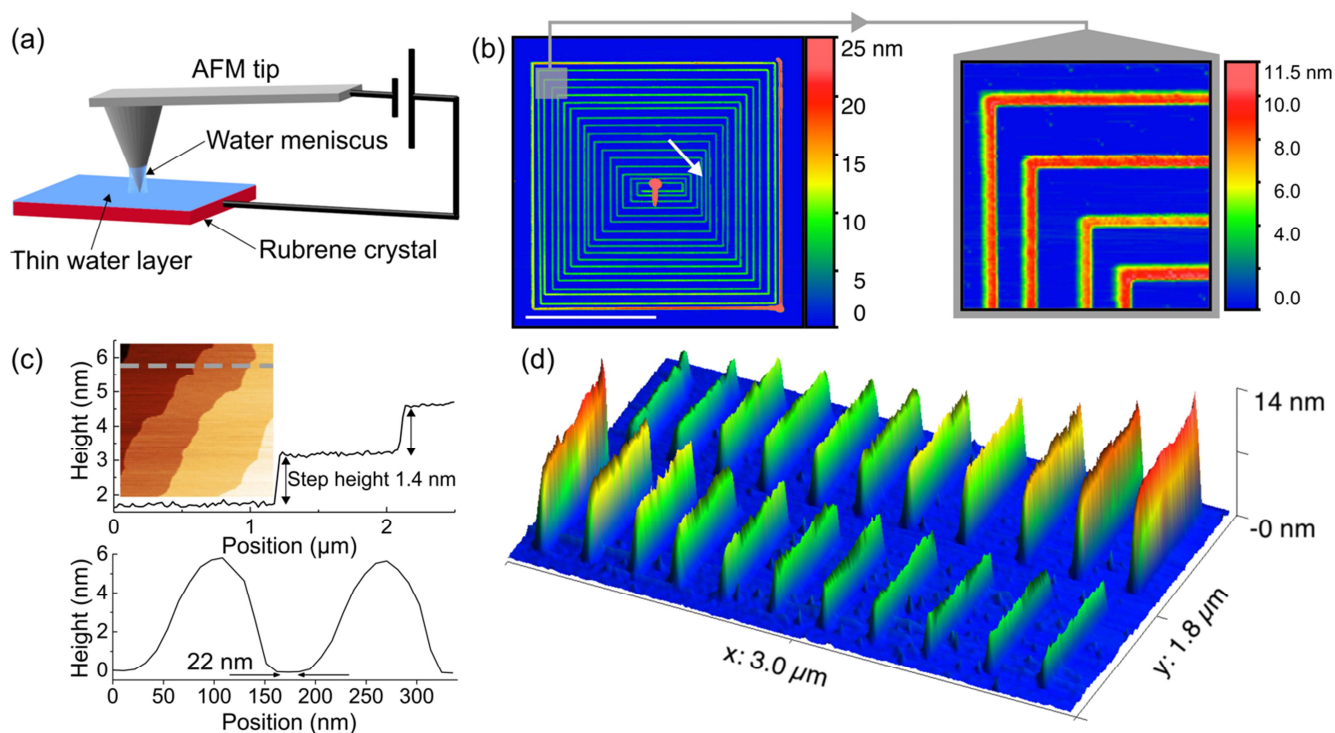
Figure 1. (a) A schematic of the AFM setup for performing LAO. A water meniscus or bridge is formed between the tip and sample surface covered by a thin water layer, and the tip is negatively biased with respect to the sample. **(b)** AFM topography of a single continuous serpentine feature of length 355 µm drawn inwards from the outside on a single crystal rubrene surface (voltage bias of -22 V, tip writing speed of 10 nm/s), over an area of approximately 10 µm by 10 µm. The white arrow points to the area where a line profile is taken and shown in (c). The white scale-bar at the bottom left corresponds to a length of 4 µm. There is a test oxide blob at the centre of the serpentine feature. A 1.4 µm by 1.4 µm area indicated by the translucent grey box is magnified to show uniform edges of the oxide features, as well as sharp and well-defined right-angled corners. **(c)** Bottom: A line profile extracted from the data in (b) showing a 22 nm gap at the surface between two oxide features. Top: For reference, a line profile of a pristine rubrene crystal surface, displaying the characteristic step edges of height ~1.4 nm, corresponding to the grey dashed line across the 2.5 µm by 2.5 µm AFM topography image in the inset (false colour vertical scale is 6.8 nm black to white). **(d)** A three-dimensional render of LAO with varying tip speed from 10-35 nm/s at a constant voltage bias of -22 V (front row) and varying voltage bias from -12 to -22 V at constant tip writing speed of 10 nm/s (back row). The data is quantitatively presented in Fig. 2.

Previously, LAO has been used either directly or as an intermediary step to fabricate circuit components and devices such as quantum point contacts [24], quantum dots [25], nanorings [26], narrow/one-dimensional channels [27,28], ferromagnetic tunnel junctions [29], transistors (including single electron and single hole transistors) [30,31] and nanowire-based devices [32] like single photon detectors [33]. A variety of materials have been the subject of study involving LAO, among them metals[34], Group IV and III-V semiconductors [27,35], two-dimensional materials [25], transition metal dichalcogenides [28] and ferromagnetic materials [29].

One criterion for the successful use of LAO in device fabrication is that the oxide feature depth exceeds the device active layer thickness, therefore the ability to accurately measure the depth of these features is important. Oxide depth characterisation is typically carried out by selectively etching the oxide feature and measuring the depth of the void that remains. However, we are not aware of etchants for selective organic oxide removal, rendering this procedure unsuitable for use on organic semiconductor systems, posing a problem for oxide depth characterisation in organic materials.

In this Article, we achieve a major step in the pursuit towards achieving direct-write oxide-based fabrication of nanoscale electronic devices on organic semiconductors, by precisely drawing electrically insulating oxide lines using LAO on the organic semiconductor crystal rubrene and characterising the dimensions, most importantly the depth. Depth characterisation is made possible by employing the recently developed conductance tomography technique [36,37], utilising contact mode conductive atomic force microscopy (CAFM) to etch through layers of the material until the insulating oxide feature disappears, and is demonstrated for the first time on organic materials. The oxide penetrates deeper than its height, and a critical electric field is identified, below which the oxide growth terminates.
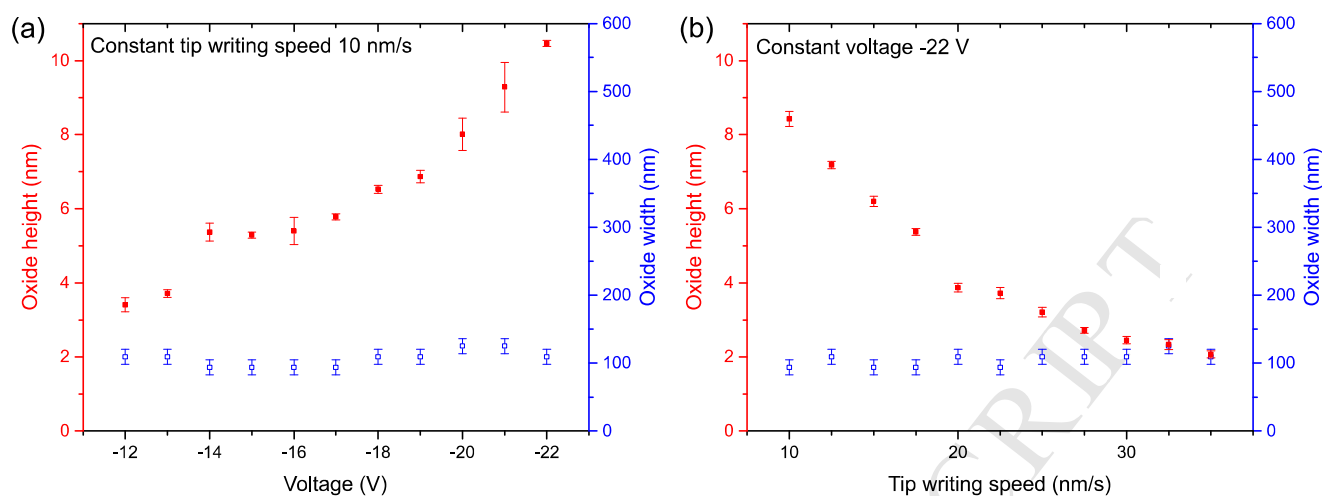
Figure 2. Dependence of mean oxide height and width on **(a)** voltage and **(b)** tip writing speed, for the oxide lines shown in Fig. 1(c). The red solid data points represent that of oxide height (left axis); the blue open data points represent oxide width (right axis). The error bars for the oxide height are one standard deviation of the measured heights along the features, while those for the oxide width are based on the position interval between adjacent line scans.

74
75 ## 2. Results & Discussion
76
77 A schematic diagram showing the experimental setup for performing LAO is shown in Fig. 1(a). In the presence of significant
78 humidity, a thin water layer is formed on the substrate surface and the AFM tip-sample interaction region is wetted typically by
79 the formation of a water meniscus in contact mode or a water bridge in non-contact/tapping mode (a sufficient voltage bias is
80 required to form the water bridge) [38]. In the setup of Fig. 1(a), the AFM tip is negatively biased with respect to the sample;
81 water molecules are dissociated and the electric field directs oxyanions into the substrate to form oxide derivatives [39]. This
82 reaction is limited to the lateral dimensions of the water meniscus or water bridge [38]. The resultant oxide is amorphous [40]
83 and less dense than the substrate, thus protrudes from the surface due to vertical volume expansion [41]. The oxide depth
84 depends on the maximum oxyanion travel into the substrate, which is determined by factors such as the electric field strength,
85 material density and interatomic/intermolecular force strength, as well as activation energies for oxyanion penetration and the
86 oxide-forming reaction. We now study the LAO process using tapping mode on the surfaces of single crystal rubrene,
87 specifically the most developed crystal face (the *ab*-plane) which displays the characteristic step heights of ~1.4 nm between
88 terraces (Fig. 1(c)). The surfaces and step edges were observed to be free from any signs of contamination. In this study, LAO
89 is performed on flat surfaces only, avoiding areas with step edges (i.e. avoiding the steps shown in Fig. 1(c)).
90
91 To realise LAO using tapping mode on rubrene crystals, a minimum relative humidity of 70 % is required, which is higher than
92 for inorganic materials (e.g. 30-40 % for Si) [38]. In addition, a very low feedback setting is required (setpoint amplitude of ~1
93 nm, from a free amplitude of ~25 nm), corresponding to a peak-to-peak oscillation amplitude of ~2 nm throughout the LAO
94 procedure, resulting in the tip being very close to the sample with a great likelihood of contact with the surface. However, such
95 a feedback setting rarely changes the surface topography; at zero voltage bias the largest effect, if observed at all, was a
96 uniform depression ~1 nm deep (corresponding to 1 molecular layer). Though the chemical composition of the oxide lines is
97 not determined, it is expected to be an oxy- and/or hydroxy- derivative of rubrene. Studies of such modified rubrene molecules
98 point towards the introduction of deep trap states [42] and unfavourable modifications of the HOMO and/or LUMO orbitals
99 which destroy π-conjugation due to, for example, a bent tetracene backbone (as in the case of rubrene endoperoxide) [43,44].
100 Importantly, CAFM confirms that the oxide features are electrically insulating, and this is the overriding characteristic of the
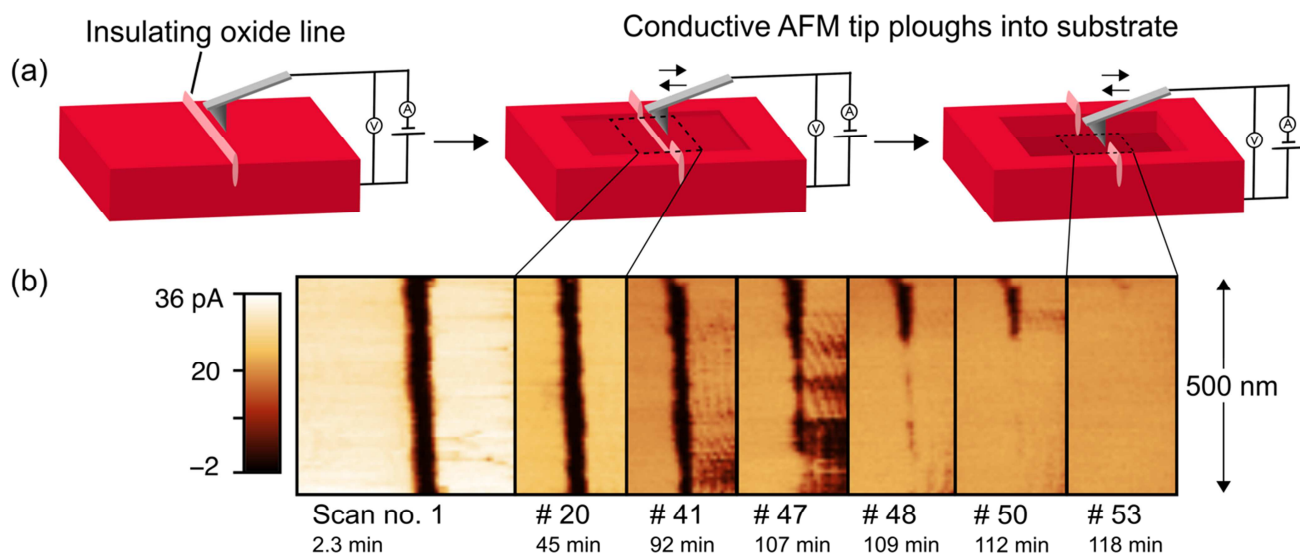101 results we present, that can be of benefit in organic nanoelectronics.
102

Figure 3. **(a)** A schematic of the utilisation of conductance tomography to determine oxide feature depth. Left: Before conductance tomography. Middle: After several layers are removed. Right: Immediately after passing the bottom of the oxide feature. **(b)** Selected CAFM data obtained during the tomography process corresponding to Experiment 5 in Fig. 5(a), in which the oxide feature was completely removed after 53 scans, as shown by the disappearance of current contrast. Raw data is presented and the current data zero offset was not corrected. Each scan was 500 nm by 500 nm, although we have cropped all but scan #1 to show more scans.

103   To demonstrate that long oxide lines can be written, a single serpentine feature of length 355 µm was drawn in one continuous
104   movement within an area of just under 10 µm by 10 µm, as shown in Fig. 1(b). Neatly drawn corners are produced upon
105   changing direction (in this case, right-angled turns). Gaps between adjacent oxide line segments were measured to be as small
106   as 22 nm at the surface (Fig. 1 (c)), demonstrating the uniformity of the line edges and, importantly, the precision that the LAO
107   technique offers. The gradual decrease in height as the serpentine feature is drawn inwards from the outside could be attributed
108   to a gradual change of the tip, probably tip wear. The width of the oxide line segments in the serpentine feature remained the
109   same along its whole length, at about 100 nm. In addition, crystal orientation was observed to not affect the LAO procedure
110   and oxide feature dimensions; for example, in the serpentine feature of Fig. 1(b) there were no observed differences in oxide
111   dimensions of lines drawn in perpendicular directions.
112
113   The effect of voltage bias and tip writing speed on oxide growth are then studied. Figure 1(d) shows the AFM topography of
114   the results obtained, in a three-dimensional render, while the graphs in Fig. 2 depict the dependence of mean oxide line height
115   and width on tip-sample voltage bias and tip writing speed. The oxide height increases with voltage bias, and decreases with tip
116   writing speed. LAO oxide growth behaviour can be explained theoretically [35] (based on the Cabrera-Mott theory of metal
117   thin film oxidation) [45], describing oxide height variation as linear with voltage bias and as log(1/speed) with tip writing
118   speed. Good agreement has been found in the case of Si [35] and Ti [46]. However, for materials such as rubrene crystals and
119   GaAs [47], despite observing an increase in oxide height with tip voltage, a log (1/speed) dependence does not produce the best
120   fit to data, indicating that the oxidation mechanism in compounds and/or molecular crystals is more complicated than suggested
121   in the model. The maximum tip writing speed is 35 nm/s, beyond which no protruding features are observed, unlike LAO in
122   other materials such as Si where tip writing speeds above 100 µm/s can be used [35].
123
124   Meanwhile, the oxide line width remained generally constant at about 100 nm, a relatively large LAO line width, independent
125   of voltage and tip writing speed. We suggest this is due to the high relative humidity requirement, aided by the low setpoint
126   amplitude. For silicon nitride AFM tips (of geometry and dimensions similar to those used in this experiment) in contact with
127   gold and silicon surfaces under 40-60 % relative humidity, it was found that the water meniscus width is on the order of 100
128   nm – 1 µm, while its height is on the order of 100 nm [48]. Similarly, relatively large water meniscus dimensions are also
129   expected in our system, whose shape and size should be unaffected by the low tip oscillation amplitude of ~2 nm peak-to-peak.
130   Thus, we suggest LAO performed on rubrene crystals in this study proceeds under a configuration involving a water meniscus
131   instead of a water bridge [38].
132
133   Next, we discuss the conductance tomography technique. Since the oxide lines are electrically insulating, a current contrast
134   between the oxide line and rubrene crystal is observed in the CAFM data, enabling the utilisation of this technique to determine
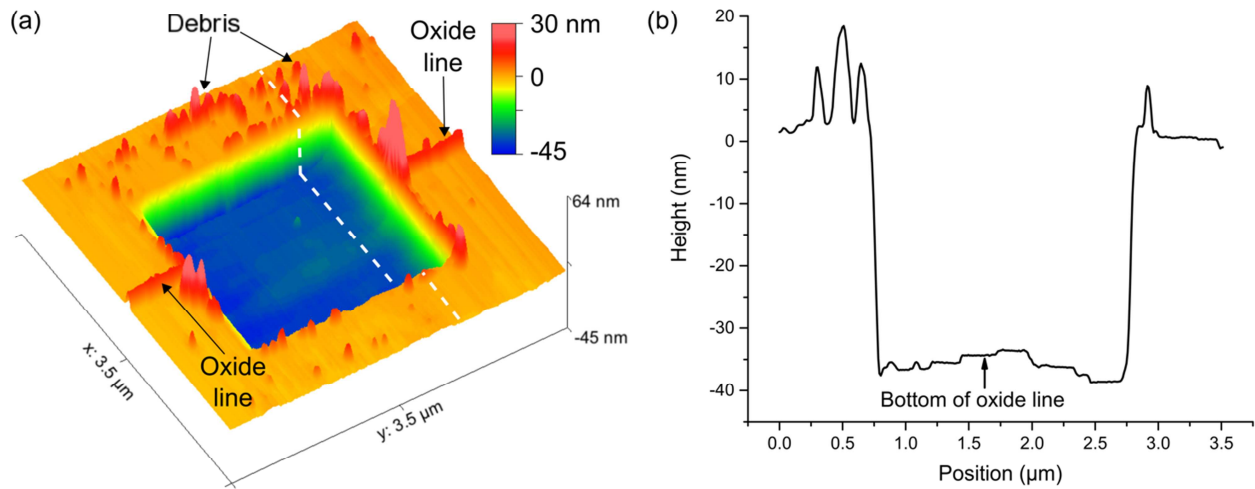
4

Figure 4. (a) A three-dimensional render of the crater corresponding to Experiment 7 in Fig. 5(a). The false colour bar is terminated at 30 nm. **(b)** A line profile taken across the crater perpendicular to the oxide line, along the white dashed line in (a), from which the oxide line depth of the oxide line is measured.

135   oxide line depths. A schematic is presented in Fig. 3(a). In order to realise conductance tomography, removal of substrate
136   material using the AFM tip is performed during contact mode CAFM imaging of an oxide feature. It involves the combination
137   of a vertically downward force (due to an increased AFM setpoint) that damages the crystalline structure to initiate an
138   indentation or crack, and the lateral movement of the tip as it scans the surface, which serves a dual function. First, the tip
139   scratches and ploughs the surface, producing debris; second, the tip sweeps the debris to the edges and out of the scanned area.
140   The tip-sample voltage bias could also influence this process. The production and removal of debris causes the formation of a
141   crater in the shape of the scanned area. Throughout this process, the simultaneously obtained current maps show a clear current
142   contrast between the insulating oxide line and the conducting rubrene crystal (Fig. 3(b)). As more material is removed, deeper
143   layers are uncovered until the current contrast disappears, indicating that the bottom of the oxide line has been reached. At this
144   point, the tomography procedure is terminated. The crater depth is then determined by imaging over a larger scan area using
145   normal feedback setpoint settings for topography imaging. A line profile is taken perpendicular to the (now removed) oxide
146   line. Figures 4(a) and 4(b) show data from a crater resulting from a conductance tomography measurement over an area of 2
147   μm by 2 μm. During tomography experiments, the exact condition of a tip will determine the number of scans required to
148   achieve certain crater depth. Even for new tips, the cantilever spring constant, tip geometry and tip blunting rate may vary,
149   potentially affecting tip penetration depth into the sample and displacement of the material during each individual scan.
150   However, these variations in material removal do not affect the final determination of oxide line depth, which is obtained from
151   an independent measurement of the crater depth.
152
153   We now report the results of conductance tomography on oxide lines of varying height. Oxide lines were drawn on two rubrene
154   crystal samples in separate sessions using different new tips. Conductance tomography was performed on nine oxide line
155   segments with heights of 5-25 nm (the tallest reproducible height using a -22 V bias is ~25 nm). Figure 5(a) shows the oxide
156   line heights and their respective depths, and Fig. 5(b) shows oxide line depth-to-height ratios as a function of oxide height. In
157   Fig. 5(a) the increase of oxide height above the surface as a function of increasing voltage is approximately matched by an
158   increase in depth of oxide below the surface. The maximum height and depth of oxide line observed in rubrene are 25 nm and
159   40 nm respectively, while the maximum heights and depths in other materials are both about 15 nm when using LAO voltages
160   of the same order of magnitude [49,50]. In rubrene crystals, the overwhelming majority of oxide lines have a depth-to-height
161   ratio of more than 1.6, and oxide lines taller than 10 nm have an even larger depth-to-height ratio (some greater than 2). The
162   oxide depth-to-height ratios in other materials are typically constant with no dependence on height, with values of 0.6 and 1 in
163   Si and GaAs respectively [41,49] (more materials tend to be within this range, e.g. Ge thin films [51] and WSe$_2$ [28]), while in
164   GaSb and a Ti film the values are higher at 2.1 and ~2.5 respectively [46,50].
165
166   At taller oxide line heights formed by higher voltages up to -22 V, specifically Experiments 8 and 9 in Fig. 5(a), there appears
167   to be a maximum limit to the oxide feature vertical extent of ~60 nm, regardless of height above the baseline. In Experiment 9,
168   a protrusion 25 nm tall is produced but the depth reaches to only 36 nm; the height-to-depth ratio plummets, corresponding to
169   the encircled data point in Fig. 5(b). Thus, it can be inferred that the LAO process terminates at or below a critical electric field
170   of about ~3×10^6 V/cm, where the field can no longer propagate oxyanions across the growing oxide. This is about three times
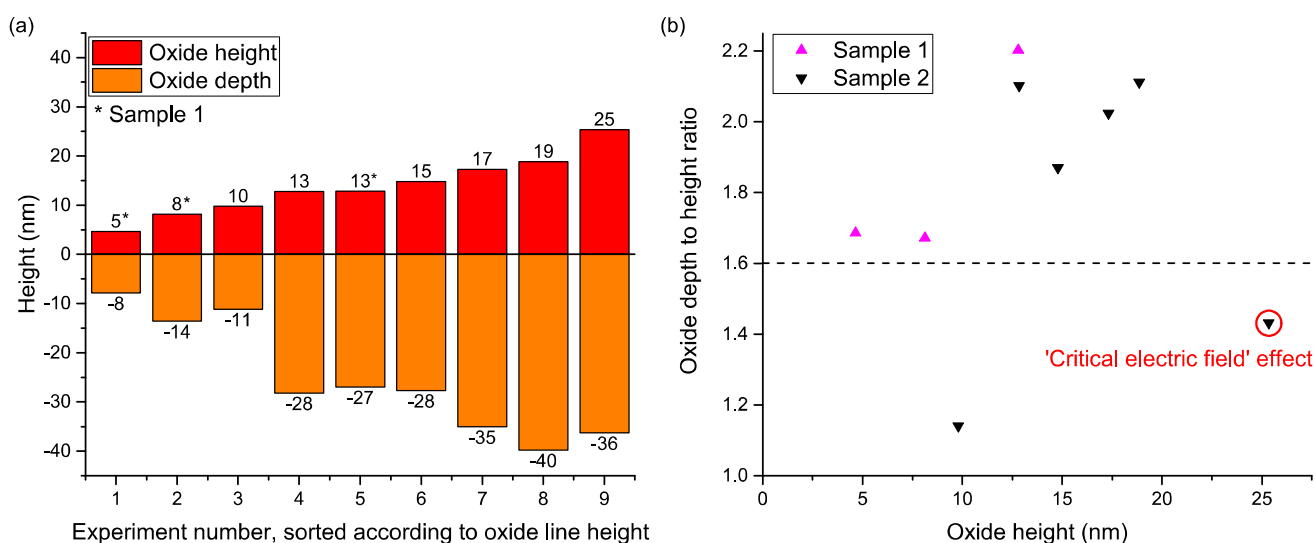
5

Figure 5. (a) A graph showing the heights and depths of nine conductance tomography experiments on oxide features produced by LAO on single crystal rubrene. Experiments performed on oxide features drawn on Sample 1 are marked with an asterisk, while the rest were from Sample 2. In producing these oxide features, the tip writing speed was kept constant at 10 nm/s while the voltage biases used were within -12 to -22 V. **(b)** A graph showing the oxide depth-to-height ratio as a function of oxide height. All oxide lines penetrate deeper than their height, and most have a depth-to-height ratio of more than 1.6. The data point encircled in red corresponds to Experiment 9 in Fig. 5(a), where the effects of a weakening electric field due to a larger oxide vertical extent are observed.

lower than the quoted range of $\sim 1 \times 10^7$ V/cm as per observations on Si and GaAs [35,49]. We note there is one anomalous data point in Figure 5(b) (oxide height of 10 nm), where the depth-to-height ratio is unexpectedly low, even less than in the case of the 'critical electric field effect'. This is likely an effect of tip wear, since multiple relatively long oxide lines are drawn in this part of the study, with the tip repeatedly approaching and withdrawing from the surface.

3. Conclusions

In summary, LAO was successfully performed on single crystal rubrene to produce precisely drawn continuous oxide features, where the height increases with voltage bias and decreases with tip writing speed. Gaps as narrow as 22 nm at the surface between two adjacent parallel oxide lines were achieved; in principle, devices of such width aligned along the highest mobility axis will have channels less than 35 rubrene molecules wide. The recently developed conductance tomography technique proved to be suitable for revealing oxide feature penetration depths. The oxide line depth exceeds the height, with depth-to-height ratio of more than 1.6 in most cases. The maximum height and depth of the oxide features exceed those reported on many materials. A critical electric field of $\sim 3 \times 10^6$ V/cm is identified, below which the oxide ceases to grow; this corresponds to a maximum oxide vertical extent of ~ 60 nm within the range of voltage bias used (up to -22 V). Importantly, the successful utilisation of this method to characterise the depth of oxide features is a major milestone in enabling the proper utilisation of LAO as a direct-write technique for fabricating electronic devices on organic semiconductors, including future one-dimensional device structures, and aid in increasing device density. Deeper oxides enable modifying deeper active layers and can be instrumental in making more multi-layered device architectures possible. The proven scaling up of this method by stamp patterning is a compelling reason to apply anodic oxidation in large-scale usage and organic electronic device mass production [6].

4. Experimental section

Rubrene single crystals were grown by physical vapour transport in a two-zone furnace (base temperature of 260 °C and sublimation temperature of 310 °C) under ultra-high purity Ar gas flow of 30 ml/min, with rubrene powder (Rubrene 99%, ACROS Organics™) as the initial source material. A second growth cycle is performed, now with rubrene single crystals as the source material, to ensure higher purity crystals are obtained. Each growth lasts about 48 hours, producing crystals with large flat surfaces corresponding to the *ab*-plane (few millimetres in the *a*-direction and more than 5 mm in the highest mobility *b*-direction). The crystals are about 300 µm thick (i.e. in the *c*-direction).

202 A Bruker Dimension Icon atomic force microscope was used to perform all AFM work, while the Gwyddion software package
203 was used to perform analysis. Topography imaging and LAO in tapping mode were performed using a standard n-type silicon
204 cantilever (~40 N/m spring constant, ~300 kHz resonance frequency). A low free amplitude of ~25 nm was used. Topography
205 imaging was done at a setpoint amplitude ~75% of the free amplitude, and LAO was performed with the feedback on at a
206 setpoint amplitude of ~5 % of the topography imaging setpoint, corresponding to an absolute amplitude of ~1 nm (larger
207 setpoints did not produce oxide lines). A constant dc voltage was applied throughout the LAO procedure, with the voltage
208 linearly ramped rapidly (0.1 s) to and from the desired voltage immediately before and after oxidation, respectively.

210 Contact mode CAFM and conductance tomography were performed using a cantilever coated with a 25-nm wear resistant
211 double layer of chromium and platinum-iridium5 alloy (~0.2 N/m spring constant, ~13 kHz resonance frequency). CAFM
212 tomography was performed at a setpoint of at least 0.5 V above the normal setpoint for topography imaging, at a maximum
213 scanning speed of 8μm/s and maximum scan size of 2 μm by 2 μm, typically using a line density of 128 lines per 2 μm. A bias
214 in the range of 2-5 V is applied to the sample to observe current contrast between conducting and insulating features, and a
215 larger scan size and slower scan speed gives the best well-defined craters possessing relatively flat bases and steep walls.

217 **Data Availability**

219 Data acquired and analysed during the current study are available from the corresponding author on reasonable request.

221 # Acknowledgements

226 # References

228 [1]   D. Tobjörk, R. Österbacka, Paper Electronics, Adv. Mater. 23 (2011) 1935–1961.
229   doi:10.1002/adma.201004692.
230 [2]   J.E. Anthony, Functionalized acenes and heteroacenes for organic electronics, Chem. Rev. 106 (2006) 5028–
231   5048. doi:10.1021/cr050966z.
232 [3]   C.J. Brabec, J.R. Durrant, Solution-processed organic solar cells, MRS Bull. 33 (2008) 670–675.
233   doi:10.1557/mrs2008.138.
234 [4]   E. Menard, M. a. Meitl, Y. Sun, J.U. Park, D.J.L. Shir, Y.S. Nam, S. Jeon, J. a. Rogers, Micro- and
235   nanopatterning techniques for organic electronic and optoelectronic systems, Chem. Rev. 107 (2007) 1117–
236   1160. doi:10.1021/cr050139y.
237 [5]   Y.K. Ryu, R. Garcia, Advanced oxidation scanning probe lithography, Nanotechnology. 28 (2017) 142003.
238   doi:10.1088/1361-6528/aa5651.
239 [6]   M. Cavallini, P. Mei, F. Biscarini, R. García, Parallel writing by local oxidation nanolithography with
240   submicrometer resolution, Appl. Phys. Lett. 83 (2003) 5286–5288. doi:10.1063/1.1633685.
241 [7]   J.E. Shaw, P.N. Stavrinou, T.D. Anthopoulos, On-Demand Patterning of Nanostructured Pentacene
242   Transistors by Scanning Thermal Lithography, Adv. Mater. 25 (2013) 552–558.
243   doi:10.1002/adma.201202877.
244 [8]   L. Li, M. Hirtz, W. Wang, C. Du, H. Fuchs, L. Chi, Patterning of Polymer Electrodes by Nanoscratching,
245   Adv. Mater. 22 (2010) 1374–1378. doi:10.1002/adma.200902941.
246 [9]   N.S. Losilla, J. Martinez, E. Bystrenova, P. Greco, F. Biscarini, R. García, Patterning pentacene surfaces by
247   local oxidation nanolithography, Ultramicroscopy. 110 (2010) 729–732.
248   doi:10.1016/J.ULTRAMIC.2010.02.040.
249 [10]   J. Takeya, M. Yamagishi, Y. Tominari, R. Hirahara, Y. Nakazawa, T. Nishikawa, T. Kawase, T. Shimoda,
250   S. Ogawa, Very high-mobility organic single-crystal transistors with in-crystal conduction channels, Appl.
251   Phys. Lett. 90 (2007) 102120. doi:10.1063/1.2711393.
252 [11]   V. Podzorov, E. Menard, A. Borissov, V. Kiryukhin, J.A. Rogers, M.E. Gershenson, Intrinsic Charge
253   Transport on the Surface of Organic Semiconductors, Phys. Rev. Lett. 93 (2004) 086602.
254   doi:10.1103/PhysRevLett.93.086602.
255 [12]   K.K. Zhang, K. Tan, C. Zou, M. Wikberg, L.E. McNeil, S.G. Mhaisalkar, C. Kloc, Control of charge
256   mobility in single-crystal rubrene through surface chemistry, Org. Electron. 11 (2010) 1928–1934.

257   doi:10.1016/j.orgel.2010.08.019.

258   [13]   H. Najafov, B. Lee, Q. Zhou, L.C. Feldman, V. Podzorov, Observation of long-range exciton diffusion in
259   highly ordered organic semiconductors., Nat. Mater. 9 (2010) 938–43. doi:10.1038/nmat2872.

260   [14]   P. Irkhin, I. Biaggio, Direct Imaging of Anisotropic Exciton Diffusion and Triplet Diffusion Length in
261   Rubrene Single Crystals, Phys. Rev. Lett. 107 (2011) 017402. doi:10.1103/PhysRevLett.107.017402.

262   [15]   L. Raimondo, S. Trabattoni, M. Moret, N. Masciocchi, M. Masino, A. Sassella, Oxidation of Crystalline
263   Rubrene Films: Evidence of an Epitaxial Native Oxide Layer, Adv. Mater. Interfaces. 4 (2017) 1700670.
264   doi:10.1002/admi.201700670.

265   [16]   R.J. Thompson, S. Fearn, K.J. Tan, H.G. Cramer, C.L. Kloc, N.J. Curson, O. Mitrofanov, Revealing surface
266   oxidation on the organic semi-conducting single crystal rubrene with time of flight secondary ion mass
267   spectroscopy., Phys. Chem. Chem. Phys. 15 (2013) 5202–7. doi:10.1039/c3cp50310k.

268   [17]   D.D.T. Mastrogiovanni, J. Mayer, A.S. Wan, A. Vishnyakov, A. V Neimark, V. Podzorov, L.C. Feldman, E.
269   Garfunkel, Oxygen incorporation in rubrene single crystals., Sci. Rep. 4 (2014) 4753.
270   doi:10.1038/srep04753.

271   [18]   R.J. Thompson, T. Bennett, S. Fearn, M. Kamaludin, C. Kloc, D.S. McPhail, O. Mitrofanov, N.J. Curson,
272   Channels of oxygen diffusion in single crystal rubrene revealed, Phys. Chem. Chem. Phys. 18 (2016)
273   32302–32307. doi:10.1039/C6CP05369F.

274   [19]   O. Mitrofanov, D. V. Lang, C. Kloc, J.M. Wikberg, T. Siegrist, W.-Y. So, M. a. Sergent, A.P. Ramirez,
275   Oxygen-Related Band Gap State in Single Crystal Rubrene, Phys. Rev. Lett. 97 (2006) 166601.
276   doi:10.1103/PhysRevLett.97.166601.

277   [20]   K.K. Zhang, K. Tan, C. Zou, M. Wikberg, L.E. Mcneil, S.G. Mhaisalkar, C. Kloc, Control of charge
278   mobility in single-crystal rubrene through surface chemistry, Org. Electron. 11 (2010) 1928–1934.
279   doi:10.1016/j.orgel.2010.08.019.

280   [21]   A.J. Maliakal, J.Y.C. Chen, W.Y. So, S. Jockusch, B. Kim, M.F. Ottaviani, A. Modelli, N.J. Turro, C.
281   Nuckolls, A.P. Ramirez, Mechanism for oxygen-enhanced photoconductivity in rubrene: Electron transfer
282   doping, Chem. Mater. 21 (2009) 5519–5526. doi:10.1021/cm902699s.

283   [22]   H. Najafov, D. Mastrogiovanni, E. Garfunkel, L.C. Feldman, V. Podzorov, Photon-assisted oxygen diffusion
284   and oxygen-related traps in organic semiconductors, Adv. Mater. 23 (2011) 981–985.
285   doi:10.1002/adma.201004239.

286   [23]   Y. Chen, V. Podzorov, Bias stress effect in "air-gap" organic field-effect transistors., Adv. Mater. 24 (2012)
287   2679–84. doi:10.1002/adma.201200455.

288   [24]   R. Held, T. Heinzel, P. Studerus, K. Ensslin, M. Holland, Semiconductor quantum point contact fabricated
289   by lithography with an atomic force microscope, Appl. Phys. Lett. 71 (1997) 2689–2691.
290   doi:10.1063/1.120137.

291   [25]   R.K. Puddy, C.J. Chua, M.R. Buitelaar, Transport spectroscopy of a graphene quantum dot fabricated by
292   atomic force microscope nanolithography, Appl. Phys. Lett. 103 (2013) 183117. doi:10.1063/1.4828663.

293   [26]   L. Weng, L. Zhang, Y.P. Chen, L.P. Rokhinson, Atomic force microscope local oxidation nanolithography
294   of graphene, Appl. Phys. Lett. 93 (2008) 093107. doi:10.1063/1.2976429.

295   [27]   N.J. Curson, R. Nemutudi, N.J. Appleyard, M. Pepper, D.A. Ritchie, G.A.C. Jones, Ballistic transport in a
296   GaAs/Al$_x$ Ga$_{1-x}$ As one-dimensional channel fabricated using an atomic force microscope, Appl. Phys. Lett.
297   78 (2001) 3466–3468. doi:10.1063/1.1374225.

298   [28]   A.I. Dago, Y.K. Ryu, R. Garcia, Sub-20 nm patterning of thin layer WSe$_2$ by scanning probe lithography,
299   Appl. Phys. Lett. 109 (2016) 163103. doi:10.1063/1.4965840.

300   [29]   Y. Tomoda, S. Kayashima, T. Ogino, M. Motoyama, Y. Takemura, J. Shirakashi, Planar-type ferromagnetic
301   tunnel junctions fabricated by SPM local oxidation, J. Magn. Magn. Mater. 310 (2007) e641–e643.
302   doi:10.1016/J.JMMM.2006.10.682.

303   [30]   S. Lüscher, A. Fuhrer, R. Held, T. Heinzel, K. Ensslin, W. Wegscheider, In-plane gate single-electron
304   transistor in Ga[Al]As fabricated by scanning probe lithography, Appl. Phys. Lett. 75 (1999) 2452–2454.
305   doi:10.1063/1.125045.

306   [31]   B. Grbić, R. Leturcq, K. Ensslin, D. Reuter, A.D. Wieck, Single-hole transistor in p-type GaAs∕AlGaAs
307   heterostructures, Appl. Phys. Lett. 87 (2005) 232108. doi:10.1063/1.2139994.

308   [32]   R. V Martínez, J. Martínez, R. Garcia, Silicon nanowire circuits fabricated by AFM oxidation
309   nanolithography, Nanotechnology. 21 (2010) 245301. doi:10.1088/0957-4484/21/24/245301.

310   [33]   C. Delacour, B. Pannetier, J.-C. Villegier, V. Bouchiat, Quantum and Thermal Phase Slips in

311   Superconducting Niobium Nitride (NbN) Ultrathin Crystalline Nanowire: Application to Single Photon
312   Detection, Nano Lett. 12 (2012) 3501–3506. doi:10.1021/nl3010397.

313 [34] Z.J. Davis, G. Abadal, O. Hansen, X. Borisé, N. Barniol, F. Pérez-Murano, A. Boisen, AFM lithography of
314   aluminum for fabrication of nanomechanical systems, Ultramicroscopy. 97 (2003) 467–472.
315   doi:10.1016/S0304-3991(03)00075-5.

316 [35] D. Stiévenard, P.A. Fontaine, E. Dubois, Nanooxidation using a scanning probe microscope: An analytical
317   model based on field induced oxidation, Appl. Phys. Lett. 70 (1997) 3272–3274. doi:10.1063/1.118425.

318 [36] M. Buckwell, L. Montesi, S. Hudziak, A. Mehonic, A.J. Kenyon, Conductance tomography of conductive
319   filaments in intrinsic silicon-rich silica RRAM, Nanoscale. 7 (2015) 18030–18035.
320   doi:10.1039/C5NR04982B.

321 [37] M. Lanza, U. Celano, F. Miao, Nanoscale characterization of resistive switching using advanced conductive
322   atomic force microscopy based setups, J. Electroceramics. 39 (2017) 94–108. doi:10.1007/s10832-017-
323   0082-1.

324 [38] R. García, M. Calleja, F. Pérez-Murano, Local oxidation of silicon surfaces by dynamic force microscopy:
325   Nanofabrication and water bridge formation, Appl. Phys. Lett. 72 (1998) 2295–2297. doi:10.1063/1.121340.

326 [39] M. Lazzarino, S. Heun, B. Ressel, K.C. Prince, P. Pingue, C. Ascoli, Atomic force microscope anodic
327   oxidation studied by spectroscopic microscopy, Appl. Phys. Lett. 81 (2002) 2842–2844.
328   doi:10.1063/1.1509121.

329 [40] D. Stiévenard, B. Legrand, Silicon surface nano-oxidation using scanning probe microscopy, Prog. Surf. Sci.
330   81 (2006) 112–140. doi:10.1016/j.progsurf.2006.01.003.

331 [41] K. Morimoto, F. Pérez-Murano, J.. Dagata, Density variations in scanned probe oxidation, Appl. Surf. Sci.
332   158 (2000) 205–216. doi:10.1016/S0169-4332(00)00017-9.

333 [42] L. Tsetseris, S.T. Pantelides, Modification of the electronic properties of rubrene crystals by water and
334   oxygen-related species, Org. Electron. Physics, Mater. Appl. 10 (2009) 333–340.
335   doi:10.1016/j.orgel.2008.12.009.

336 [43] X. Song, L. Wang, Q. Fan, Y. Wu, H. Wang, C. Liu, N. Liu, J. Zhu, D. Qi, X. Gao, A.T.S. Wee, Role of
337   oxygen incorporation in electronic properties of rubrene films, Appl. Phys. Lett. 97 (2010) 1–4.
338   doi:10.1063/1.3466914.

339 [44] S. Sinha, C.-H. Wang, M. Mukherjee, T. Mukherjee, Y.-W. Yang, Oxidation of Rubrene Thin Films: An
340   Electronic Structure Study, Langmuir. 30 (2014) 15433–15441. doi:10.1021/la503357t.

341 [45] N. Cabrera, N.F. Mott, Theory of the oxidation of metals, Reports Prog. Phys. 12 (1949) 308.
342   doi:10.1088/0034-4885/12/1/308.

343 [46] R.J.M. Vullers, M. Ahlskog, M. Cannaerts, C. Van Haesendonck, Field induced local oxidation of Ti and
344   Ti/Au structures by an atomic force microscope with diamond coated tips, J. Vac. Sci. Technol. B
345   Microelectron. Nanom. Struct. 17 (1999) 2417. doi:10.1116/1.591104.

346 [47] J. Červenka, R. Kalousek, M. Bartošík, D. Škoda, O. Tomanec, T. Šikola, Fabrication of nanostructures on
347   Si(1 0 0) and GaAs(1 0 0) by local anodic oxidation, Appl. Surf. Sci. 253 (2006) 2373–2378.
348   doi:10.1016/J.APSUSC.2006.03.095.

349 [48] B.L. Weeks, M.W. Vaughn, J.J. Deyoreo, Direct imaging of meniscus formation in atomic force microscopy
350   using environmental scanning electron microscopy, Langmuir. 21 (2005) 8096–8098.
351   doi:10.1021/la0512087.

352 [49] R. Nemutudi, N.J. Curson, N.J. Appleyard, D.A. Ritchie, G.A.C. Jones, Modification of a shallow 2DEG by
353   AFM lithography, Microelectron. Eng. 57–58 (2001) 967–973. doi:10.1016/S0167-9317(01)00478-6.

354 [50] S. Sasa, T. Ikeda, C. Dohno, M. Inoue, Atomic Force Microscope Nanofabrication of InAs/AlGaSb
355   Heterostructures, Jpn. J. Appl. Phys. 36 (1997) 4065–4067. doi:10.1143/JJAP.36.4065.

356 [51] A.B. Oliveira, G. Medeiros-Ribeiro, A. Azevedo, Submicron fabrication by local anodic oxidation of
357   germanium thin films, Nanotechnology. 20 (2009) 345301. doi:10.1088/0957-4484/20/34/345301.

358

Author Contributions
M.K. and N.C. conceived the experiments, M.K. prepared the samples and conducted the experiments, M.K. and N.C. analysed the results. M.K. wrote the main manuscript and prepared all figures. All authors reviewed and approved the manuscript.

Additional information
Competing interests
The authors declare no competing interests.

- Oxide nanopatterning on organic semiconductor crystals (~22 nm between oxide lines)
- Unique conductance tomography technique reveals oxide depths without using etchants
- Insulating oxides potentially suitable for patterning of organic nanoelectronics